International Journal for Multiscale Computational Engineering, 4(1)95–114(2006)

Multiscale Analysis of Adiabatic Shear Bands in Tungsten Heavy Alloy Particulate Composites

R. C. Batra & B. M. Love

Department of Engineering Science and Mechanics, MC 0219, Virginia Polytechnic Institute and State University, Blacksburg, VA 24061

ABSTRACT

We use a multiscale approach to analyze adiabatic shear bands in a tungsten heavy alloy particulate composite deformed in plane strain tension at a nominal strain rate of 5000/s. Fifty μm diameter circular tungsten particulates are assumed to be randomly distributed and perfectly bonded to the nickel-iron matrix. The volume fraction of particulates equals 50%. We first analyze transient coupled thermomechanical deformations of a homogenized body with values of thermophysical material parameters equivalent to those of the particulate composite. Time histories of deformation variables on the bounding surfaces of the centrally located 2 mm × 2 mm subregion of the 10 mm × 10 mm region are recorded. Boundary conditions of surface tractions and temperature rather than of velocities and temperature are then used to analyze plane strain coupled thermomechanical deformations of the 2 mm × 2 mm composite in which tungsten particulates are randomly distributed in the central 1 mm × 1 mm subregion of the 2 mm × 2 mm region with the remaining part comprised of the equivalent homogeneous material of the 10 mm × 10 mm body. It is found that the multiscale analysis of the problem gives an adiabatic shear band initiation time of ∼ 22 μs as compared to ∼ 58 μs in the equivalent homogenized body and ∼ 50 μs in the macroanalysis of deformations of the 1 mm × 1 mm region containing a randomly distributed 50% volume fraction of 50 μm diameter tungsten particulates.

KEY WORDS

multiscale analysis, finite element solution, thermoviscoplasticity, microporous materials, particulate composite

1. INTRODUCTION

An adiabatic shear band (ASB) is a narrow region, usually a few micrometers wide, of intense plastic deformation that forms in most materials deformed at high strain rates. Even though heat conduction plays a significant role during the development of an ASB, it is termed adiabatic since there is not enough time for the heat to be conducted away from the shear banded region. The analysis of ASBs is important because they precede ductile fracture and play an important role in penetration problems. Even though the initiation, development, and propagation of ASBs have been extensively studied in homogeneous materials (e.g., see the two books by Bai and Dodd [1] and Wright [2]; the two volumes edited by Perzyna [3], and Batra and Zbib [4]; the review paper of Tomita [5]; and special issues of three journals edited by Armstrong *et al.* [6], Batra *et al.* [7], and Zbib *et al.* [8]), there are very few studies on ASBs in particulate composites. For a particulate composite replaced by an equivalent inhomogeneous thermoviscoplastic body, Batra and Love [9] and Charalambakis and Baxevanis [10] have studied the localization of deformation into ASBs.

Pressure/shear plate impact experiments on a tungsten heavy alloy (WHA) have shown that the two-phase composite is more susceptible to adiabatic shear banding than either one of its constituents [11,12]; a similar conclusion was drawn in [9]. Bose *et al.* [13], Kim *et al.* [14] and Wei *et al.* [15] have scrutinized the influence of microstructural details, such as the particulate shape and size and the volume fraction of particulates, on ASB formation in WHAs. Dick *et al.* [16] have performed reverse ballistic tests on cylindrical rods of WHAs. They found that an ASB originated from a point on the rod's mantle where the mushroomed head transitioned into the cylindrical portion, and propagated inward. Tungsten grains in the path of the ASB were severely distorted. Batra and Wilson [17] and Stevens and Batra [18] have analyzed, by the finite element method (FEM), transient thermomechanical deformations of a rapidly moving cylindrical WHA rod striking a stationary smooth rigid flat surface. Stevens and Batra [18] found that enhanced thermal softening of the material resulted in the formation of ASBs at approximately the same location as that observed by Dick *et al.* [16]. Whereas Batra and Wilson [17] randomly sprinkled nickel-iron (NiFe) particles in the tungsten (W) matrix, Stevens and Batra [18] modeled the rod material as homogeneous and isotropic.

Zhou [19] has used the FEM to study ASBs in transient coupled thermomechanical simple shearing deformations of a WHA containing circular W particulates perfectly bonded to the NiFe matrix. An ASB initiated from a notch tip introduced to simulate the collective effect of numerous microvoids and other defects that may be present in a WHA. Here, we use a multiscale analysis to analyze transient plane strain coupled thermomechanical deformations of a microporous WHA. We presume that W particulates are randomly distributed in the NiFe matrix, and they are in perfect mechanical and thermal contact with the matrix. Numerous inhomogeneities introduced by the tungsten/matrix interfaces interact with each other to determine when and where ASBs initiate. Three random distributions and one ordered distribution of particulates are studied.

The multiscale approach adopted here and described above in the Abstract attempts to incorporate the effect of the microstructure on the macroscopic deformations of the WHA, and bridge the length scale from the mesolevel to the continuum level. Ghoneim *et al.* [20], among others, have reviewed techniques to bridge length scales from the atomistic to the continuum level. Belak [21] has outlined a technique to bridge the length scale from the molecular to the continuum level for high strain-rate

fracture mechanic problems. Kadowaki and Liu [22] have developed a multiscale FE technique that starts with a concurrent discretization of the entire domain into coarse and fine FE meshes. A bridging term is constructed to account for the information common to the two meshes. They applied the technique to analyze the localization of deformation in mechanical deformations of a micropolar continuum. The multiscale approach used here derives time histories of boundary conditions for the fine scale analysis from the coarse scale analysis; the former includes microstructure of the WHA and the latter smears it into an equivalent homogeneous body.

2. FORMULATION OF THE PROBLEM

2.1 Governing Equations

We assume that the particulate and the matrix materials can be modeled as isotropic, microporous, and thermo-elasto-viscoplastic. We use rectangular Cartesian coordinates and the referential description of motion to describe their finite plane strain transient coupled thermomechanical deformations. Deformations of each constituent and of the composite body are governed by Eqs. (1)–(4) expressing, respectively, the balance of mass, the balance of linear momentum, the balance of moment of momentum, and the balance of internal energy.

$$\rho(1-f)J = \rho_0(1-f_0) \tag{1}$$

$$\rho_0(1-f_0)\dot{v}_i = T_{i\alpha,\alpha},\ i,j=1,2,\ \alpha=1,2 \tag{2}$$

$$T_{i\alpha}F_{j\alpha} = T_{j\alpha}F_{i\alpha} \tag{3}$$

$$\rho_0(1-f_0)\dot{e} = -Q_{\alpha,\alpha} + T_{i\alpha}\dot{F}_{i\alpha} \tag{4}$$

Here, ρ is the present mass density, f the porosity (i.e., the volume fraction of voids), $J = \det \mathbf{F}$, $F_{i\alpha} = x_{i,\alpha} = \partial x_i/\partial X_\alpha$ the deformation gradient, $\mathbf{x}$ the present position at time t of a material particle located at the place $\mathbf{X}$ in the reference configuration, $\mathbf{T}$ the first Piola-Kirchhoff stress tensor, e the specific internal energy, $\mathbf{Q}$ the present heat flux measured per unit reference area, $\mathbf{v}$ the velocity of a material particle, a superimposed dot indicates the material time derivative, and a repeated index implies summation over the range of the index. Greek indices refer to coordinates in the reference configuration, and Latin indices to coordinates in the present configuration. The porosity f is assumed to be uniformly distributed in each constituent, and can be regarded as a measure of the damage.

We assume that the strain-rate tensor $\mathbf{D}$, defined by $D_{ij} = (v_{i,j} + v_{j,i})/2$, $v_{i,j} = \partial v_i/\partial x_j$, has the additive decomposition into an elastic part $\mathbf{D}^e$, a plastic part $\mathbf{D}^p$, and a thermal part $\hat{\alpha}\dot{\theta}\mathbf{1}$, viz., $\mathbf{D} = \mathbf{D}^e + \mathbf{D}^p + \hat{\alpha}\dot{\theta}\mathbf{1}$. Here, $\hat{\alpha}$ is the coefficient of thermal expansion, θ the temperature rise, and $\mathbf{1}$ the identity tensor. Equations (1)–(4) are supplemented with the following constitutive relations.

$$\dot{\sigma}_{ij} + \sigma_{ik}W_{kj} + \sigma_{jk}W_{ki} = \frac{E(1-f)}{1+\nu}D^e_{ij} + \frac{E(1-f)\nu}{(1+\nu)(1-2\nu)}D^e_{kk}\delta_{ij} \tag{5}$$

$$\dot{e} = c\tau\ddot{\theta} + c\dot{\theta} + \frac{1}{\rho(1-f)}\sigma_{ij}D^e_{ij}$$
$$T_{i\alpha} = J\sigma_{ij}(F^{-1})_{\alpha j} \tag{6}$$

$$q_i = -\kappa\left(1-\tfrac{3}{2}f\right)\theta_{,i},\ Q_\alpha = Jq_i(F^{-1})_{\alpha i} \tag{7}$$

$$\phi \equiv \frac{\sigma_e^2}{\sigma_y^2} - 1 + 2f^*\beta_1\cosh\left(\frac{3\beta_2\tilde{p}}{2\sigma_y}\right) - \beta_1^2(f^*)^2 = 0$$
$$\sigma_e^2 = \frac{3}{2}\sigma'_{ij}\sigma'_{ij},\quad i,j=1,2,3 \tag{8}$$

$$D^p_{ij} = \dot{\lambda}\frac{\partial\phi}{\partial\sigma_{ij}} = \dot{\lambda}\left[\frac{3\sigma'_{ij}}{\sigma_y^2} - \frac{f^*\beta_1\beta_2}{\sigma_y}\sinh\left(\frac{3\beta_2\tilde{p}}{2\sigma_y}\right)\delta_{ij}\right]$$
$$\sigma'_{ij} = \sigma_{ij} + p\delta_{ij} \tag{9}$$

$$p = -(\sigma_{11}+\sigma_{22}+\sigma_{33})/3,\ \bar{p} = pH(-p-0) \quad (10)$$

$$\dot{\lambda} = \begin{cases} \dfrac{(1-f)\sigma_y \dot{\varepsilon}_e^p}{\sigma_{ij}\dfrac{\partial \phi}{\partial \sigma_{ij}}}, & \text{if } \phi = 0 \text{ and } \dot{\phi} \geq 0 \\ 0 & \text{when either } \phi < 0 \\ & \text{or } \phi = 0 \text{ and } \dot{\phi} < 0 \end{cases} \quad (11)$$

$$\dot{f} = (1-f)D_{ii}^p + \frac{f_2 \dot{\varepsilon}_e^p}{s_2\sqrt{2\pi}} e^{-\frac{1}{2}\left(\frac{\varepsilon_e^p - \varepsilon_n}{s_2}\right)^2} H(-p-0) \quad (12)$$

$$f^* = \begin{cases} f,\ f \leq f_c \\ f_c + \dfrac{f_u - f_c}{f_f - f_c}(f - f_c),\ f > f_c \end{cases} \quad (13)$$

$$\sigma_y = (A + B(\varepsilon_e^p)^n)\left[1 + \tilde{C}\, ln\left(\frac{\dot{\varepsilon}_e^p}{\dot{\varepsilon}_0^p}\right)\right] \times \left[1 - \left(\frac{\theta - \theta_r}{\theta_m - \theta_r}\right)^m\right] \quad (14)$$

The left-hand side of Eq. (5) equals the Jaumann derivative of the Cauchy stress tensor σ, $W_{ij} = (v_{i,j} - v_{j,i})/2$ is the spin tensor, E Young's modulus, ν Poisson's ratio, c the specific heat, τ the thermal relaxation time, κ the thermal conductivity of the solid material, and θ the present temperature of a material particle. Constitutive relation (5) implies that each constituent is being modeled as an isotropic hypoelastic material. Replacing the Jaumann derivative of σ by another objective stress rate will change the constitutive description of the material. However, Batra and Jaber [23] found that it does not alter the ASB initiation time in a homogeneous thermoviscoplastic material. $\phi = 0$ describes the yield surface proposed by Gurson [24] for a porous material, p is the hydrostatic pressure, and f^* the modified value of porosity given by (13). Gurson's yield surface is based on quasi-static analysis with the matrix material modeled as rigid perfectly plastic and obeying von Mises yield criterion. Constants β_1 and β_2, introduced by Tvergaard [25], provide a better fit of results computed from a FE analysis of the formation of ASBs in a plate having an array of large cylindrical voids with test observations, and $\dot{\lambda}$ is the factor of proportionality defined by (11); $\dot{\lambda} > 0$ only when the material point is deforming plastically, σ_y is the current yield stress of the material whose dependence on the effective plastic strain ε_e^p, the effective plastic strain rate $\dot{\varepsilon}_e^p$, and the temperature θ is described by the Johnson-Cook [26] relation (14) in which A, B, $\tilde{C}$, $\dot{\varepsilon}_0^p$, and m are material parameters, θ_r the room temperature, and θ_m the melting temperature of the material. Parameters B and n characterize the strain hardening of the material, $\tilde{C}$ and $\dot{\varepsilon}_0^p$ the strain-rate hardening, and the last factor on the right-hand side of (14) its thermal softening. Equation (12) gives the evolution of porosity; the first term on its right-hand side is derived by assuming that the matrix is incompressible and the elastic dilatation is negligible as compared to the plastic dilatation, and the second term is the strain-based nucleation of voids introduced by Chu and Needleman [27]. f_2, s_2, and ε_n are material parameters; the rate of nucleation of voids is highest when ε_e^p equals ε_n and decays exponentially with the difference between ε_e^p and ε_n. H is the Heaviside step function. We have thus assumed that new voids nucleate only when the hydrostatic stress is tensile. To account for the coalescence of neighboring voids, Tvergaard and Needleman [28] enhanced the porosity, as given by Eq. (13), after it reaches its critical value f_c. In Eq. (13), f_f is the porosity at ductile fracture, and $f_u = 1/\beta_1$ is the porosity when the yield surface has shrunk to a point. Equations (8) and imply that the radius of the von Mises yield

surface increases due to strain- and strain-rate hardening of the material but decreases due to the softening induced by the temperature rise and the increase in porosity. The degradation of material properties due to the damage, taken here as synonymous with the porosity, is indicated by Eqs. (5)–(8). The affine variation with the porosity of Young's modulus, the bulk modulus, the stress-temperature coefficient, and the heat capacity implies that the rule of mixtures has been employed to find their effective values; the expression for the thermal conductivity in Eq. (7) is due to Budiansky [29]. The interaction, if any, among neighboring voids has been tacitly ignored. Jiang and Batra [30], among others, have considered this interaction. The shrinkage of the yield surface due to an increase in porosity described by Eq. (8) can be seen by plotting the yield surface for two different values of f while keeping other variables fixed.

Substitution for $\dot{e}$ and q_i from Eqs. (6) and (7) into Eq. (4) gives the following hyperbolic heat equation:

$$\rho_0(1-f_0)c(\tau\ddot{\theta}+\dot{\theta}) = \left[\kappa\left(1-\tfrac{3}{2}f\right)\theta_{,\alpha}\right]_{,\alpha} + J\sigma_{ij}D^p_{ij} \qquad (15)$$

The term $J\sigma_{ij}D^p_{ij}$ equals the heating due to plastic working per unit volume in the reference configuration; thus, the Taylor-Quinney parameter has been taken as 1. Except for a delay in the time of initiation of an ASB, other results remain unaffected by a lower value of the Taylor-Quinney factor. The form (15) of the hyperbolic heat equation is due to Cattaneo [31] and Vernotte [32]. The thermal relaxation time τ in it represents the time required to establish a steady state of heat conduction in an element suddenly exposed to heat flux. For a typical steel, $\tau = 1 \times 10^{-12}$s, and $\tau \simeq 25 \times 10^{-12}$s for copper. Batra and Lear [33] and Batra and Chen [34] found that the finiteness of the thermal wave speed affects the ASB initiation time in a typical steel, and the spacing between adjacent shear bands only when $\tau \geq 10^{-6}$s. Batra [35] considered higher-order spatial and temporal gradients of temperature and derived a heat equation that admits finite speeds of thermal waves. However, in such a material either a thermal wave propagates with a finite speed or the linearized problem has a unique solution. Ideally, one would like to have both.

We note that Batra and Kim [36], Batra and Jaber [23], and Batra and Chen [34,37] have analyzed different aspects of shear banding with four different thermoviscoplastic relations, namely, the Johnson-Cook [26], the Litonski-Batra (e.g., see Batra [38]), the Bodner-Partom [39], and a power law. These relations were calibrated to give nearly the same effective stress versus the effective strain curve during homogeneous deformations of the body. However, during inhomogeneous deformations, each one of the relations gave qualitatively similar but quantitatively different results. The decision to use the Johnson-Cook relation here is based on the availability of values of thermomechanical parameters for tungsten and nickel-iron.

2.2 Initial and Boundary Conditions

The body is initially at rest, stress free, at a uniform temperature, has zero rate of change of temperature, and a prescribed initial porosity. Thus,

$$\begin{aligned} &\mathbf{x}(\mathbf{X},0)=\mathbf{X},\ \mathbf{v}(\mathbf{X},0)=\mathbf{0},\ \theta(\mathbf{X},0)=\theta_0 \\ &\dot{\theta}(\mathbf{X},0)=0,\ \rho(\mathbf{X},0)=\rho_0(\mathbf{X}),\ \boldsymbol{\sigma}(\mathbf{X},0)=\mathbf{0} \\ &\varepsilon^p_e(\mathbf{X},0)=0,\ f(\mathbf{X},0)=f_0(\mathbf{X}),\ \mathbf{X}\in\Omega \end{aligned} \qquad (16)$$

Here, Ω is the region occupied by the body in the reference configuration.

We assume that the body is prismatic, having a uniform cross section, and the volume fractions of constituents, initial conditions, and

boundary conditions are independent of the axial coordinate. We thus assume that a plane strain state of deformation prevails in the body. Furthermore, for the body deformed in simple tension, the cross section is square of side $2H$, and thermomechanical deformations are assumed to be symmetric about the two centroidal axes. Thus, the compositional profile has been tacitly assumed to be symmetric about the two centroidal axes.

Tensile deformations of one-quarter of the cross section, shown in Fig. 1(a), are analyzed. Boundary conditions (17), listed below, arising from the symmetry of deformations are imposed at points on the centroidal axes $X_1 = 0$ and $X_2 = 0$. The vertical surface $X_1 = H$ is taken to be traction free and thermally insulated; see Eq. (17). Normal velocity, null tangential tractions, and zero heat flux are prescribed on the top horizontal surface $X_2 = H$; these are given by Eq. (17). The prescribed normal velocity, given by Eq. (17), increases linearly with time to its steady-state value v_0 in 1 μs and is then held fixed.

$$
\begin{aligned}
&T_{21} = T_{11} = 0,\ Q_1 = 0 \quad \text{on} \quad X_1 = H \\
&T_{21} = 0,\ v_1 = 0,\ Q_1 = 0 \quad \text{on} \quad X_1 = 0 \\
&T_{12} = 0,\ v_2 = 0,\ Q_2 = 0 \quad \text{on} \quad X_2 = 0 \\
&T_{12} = 0,\ Q_2 = 0, \\
&v_2 = \begin{cases} v_0 t,\ 0 \le t \le 1\ \mu\text{s} \\ v_0, t \ge 1\ \mu\text{s} \end{cases} \quad \text{on} \quad X_2 = H
\end{aligned}
\tag{17}
$$

2.3 Interface Conditions

It is assumed that during the entire deformation process, the tungsten particulates are both mechanically and thermally perfectly bonded to the NiFe matrix. Thus,

$$
[\mathbf{u}] = \mathbf{0}, [\theta] = 0,\ [T_{i\alpha} N_\alpha] = 0,\ [Q_\alpha N_\alpha] = 0 \quad \text{on} \quad \Gamma \tag{18}
$$

where $\mathbf{N}$ is an outward unit normal, in the reference configuration, to the interface Γ between

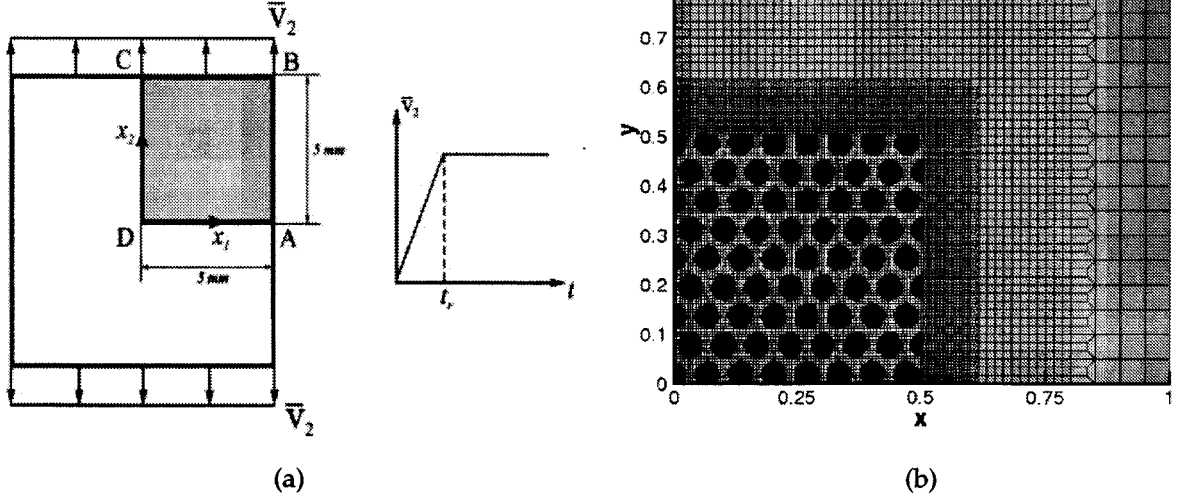

(a) (b)

FIGURE 1. Schematic sketch of the plane strain tension problem

a particulate and the matrix, and the square bracket indicates the jump of a quantity across the interface Γ between a particulate and the matrix.

2.4 Material Properties for the Equivalent Homogenized Body

There are no micromechanics-based relations available to compute values of all material parameters of a composite comprised of thermo-elasto-viscoplastic constituents. Values of E, ν, κ, α, ρ, and c for the equivalent homogenized medium can be computed by using a micromechanics-based model such as that proposed by Hill [40] and Mori and Tanaka [41], but those of A, B, $\tilde{C}$, m, n, and θ_m cannot be so found. We note that the melting temperature θ_m for the composite will equal the lowest temperature at which one of its constituents melts. The value of θ_m for the equivalent homogenized medium equals a ficticious number obtained by fitting the Johnson-Cook relation (14) to the data from either physical or numerical experiments. Numerical plane strain tension tests on representative volume elements (RVEs) of different sizes containing varying volume fractions of random and/or ordered arrangements of particulates of circular cross section were performed. Values of E, κ, α, B, $\tilde{C}$, n, and θ_m obtained from these were found to differ by at most 10% from their values computed by the rule of mixtures. According to this rule, the value P of a material parameter for a mixture comprised of two constituents with volume fractions V_1^f and V_2^f and values P_1 and P_2 of the material parameter is given by

$$P = V_1^f P_1 + V_2^f P_2 = (1 - V_2^f) P_1 + V_2^f P_2 \quad (19)$$

It gives exact values of the mass density and the heat capacity, and is simple to use. It ignores interactions among adjacent particulates, their shapes and sizes, and their distribution in the matrix.

Suquet [42] has given a closed-form expression for the quasi-static yield stress A of an isotropic homogenized body made of isotropic elastic perfectly plastic constituents. The estimate of the yield stress involves the effective shear modulus of the composite. For the W/NiFe composite studied here, the difference in the effective yield stress computed from Suquet's expression with the shear modulus derived from the Mori-Tanaka technique and that obtained by the rule of mixtures is less than 10%.

Here, the rule of mixtures, Eq. (19), has been used to ascertain values of material parameters of the W/NiFe composite.

2.5 Semidiscrete Formulation of the Problem

Equations (5), (6), and (3) imply that the balance of moment of momentum (3) is identically satisfied. The present mass density can be computed from Eq. (1) if the deformation gradient and the current value of the porosity are known. Thus, the dependent variables to be solved for are $\mathbf{x}$, f, and θ, and the independent variables are $\mathbf{X}$ and t. Equations (2) and (15) are second-order coupled nonlinear hyperbolic partial differential equations for $\mathbf{x}$ and θ. These cannot be written explicitly in terms of $\mathbf{x}$ and θ since $\mathbf{T}$ is given by (6) and $\dot{\sigma}$ by (5), which involves $\mathbf{D}^p$ and θ. We solve the problem numerically by the FEM.

We first introduce an auxiliary variable $\xi = \dot{\theta}$. Let $\psi_1, \psi_2, \ldots, \psi_n$ be the FE basis functions defined on Ω. We write

$$v_i = \sum_{A=1}^{\text{nodes}} \psi_A(\mathbf{X}) \tilde{v}_{Ai}(t), \quad w_i = \sum_{A=1}^{\text{nodes}} \psi_A(\mathbf{X}) c_{Ai}$$
$$\theta = \sum_{A=1}^{\text{nodes}} \psi_A(\mathbf{X}) \tilde{\theta}_A, \quad \xi = \sum_{A=1}^{\text{nodes}} \psi_A(\mathbf{X}) \tilde{\xi}_A, \quad i = 1, 2 \quad (20)$$

Here, $\tilde{v}$ is the vector of velocities of nodes, $\tilde{\theta}$ the vector of nodal temperatures, $\tilde{\xi}$ the vector of rate of change of temperature at the nodes, and c_{Ai} are constants. Following the usual procedure, e.g., see [43], we get

$$\mathbf{M}\dot{\tilde{v}} = -\mathbf{F}^{\text{int}},\ \dot{\theta} = \tilde{\xi},\ \theta\mathbf{H}\dot{\tilde{\xi}} = \mathbf{F}^{\theta} + \tilde{\mathbf{Q}} \tag{21}$$

where

$$\begin{aligned} M_{AB} &= \int_{\Omega} \rho_0(1-f_0)\psi_A\psi_B d\Omega, \\ F^{\text{int}}_{Ai} &= \int_{\Omega} \psi_{A,\alpha} T_{i\alpha} d\Omega \\ H_{AB} &= \int_{\Omega} \rho_0 c(1-f_0)\psi_A\psi_B d\Omega, \\ F^{\theta}_{A} &= \int_{\Omega} \kappa\left(1-\tfrac{3}{2}f\right)\theta_{,\alpha}\psi_{A,\alpha} d\Omega \\ Q_A &= \int_{\Omega} \psi_A J\,\text{tr}(\boldsymbol{\sigma}\mathbf{D}^p) d\Omega. \end{aligned} \tag{22}$$

Note that the natural boundary conditions of zero heat flux on all bounding surfaces and null surface tractions on $X_1 = H$, zero tangential tractions on $X_2 = 0$, H, and $X_1 = 0$, have been embedded in Eqs. (21). For nonzero surface tractions and nonvanishing heat flux prescribed on a part of the boundary, Eqs. (21) and (22) are suitably modified.

We solve Eq. (14) for $\dot{\varepsilon}^p_e$ in terms of σ_y, ε^p_e, and θ, and integrate the resulting equation along with Eqs. (5) and (12) at the integration (or Gauss quadrature) points. Recall that $\dot{\varepsilon}^p_e > 0$ only when a material point is deforming plastically as signified by the satisfaction of Eq. (8); otherwise $\dot{\varepsilon}^p_e = 0$. A weak form of equation $\dot{\mathbf{x}} = \mathbf{v}(\mathbf{X}, t)$ is also derived. We thus get coupled nonlinear ordinary differential equations

$$\dot{\mathbf{d}} = \mathbf{F} \tag{23}$$

where $\mathbf{d}$ is the vector of unknowns and $\mathbf{F}$ is the force vector that depends on time t and $d(t)$. The six unknowns at a node are $\{x_1, x_2, v_1, v_2, \theta, \xi\}$, and the dimension of vector $\mathbf{d}$ equals six times the number of nodes. Furthermore, unknowns at a quadrature point are $\{\sigma_{11}, \sigma_{22}, \sigma_{12}, \sigma_{33}, f, \varepsilon^p_e\}$. Thus, the total number of coupled ordinary differential equations to be integrated equal 6 (number of nodes) $+6 \times 4\times$ (number of elements) for a 2×2 integration rule. Batra and Jaber [23] employed a similar technique to numerically solve the coupled thermoviscoplastic problem. They used a FE mesh comprised of triangular elements and the one-point integration rule to compute the domain integrals.

3. COMPUTATION OF RESULTS

A computer code employing four-node isoparametric quadrilateral elements has been developed. Integrals in Eq. (22) over each element are evaluated by using the 2×2 Gauss quadrature rule. Should a FE span two materials, values of the material parameters at the Gauss quadrature point are used. Batra [44] used this procedure for analyzing finite static deformations of an inhomogeneous cylinder made of a Mooney-Rivlin material and showed that computed results matched well with the analytical solution. The coupled nonlinear ordinary differential equations (23) are integrated with respect to time t by using the subroutine LSODE (Livermore solver for ordinary differential equations) that can be downloaded free from the internet. It adaptively adjusts the time step and the order of the integration scheme so as to compute a stable solution within the prescribed absolute and relative tolerances. Because of the large number of nodes in the FE mesh, the Adams-Moulton integration method obtained by setting $MF = 10$ in LSODE is employed. Variables RTOL and ATOL that specify the relative and the absolute tolerances in the computed solution are assigned values 10^{-6} and 10^{-6}, respectively.

Both the mechanical and the thermal problems are hyperbolic. Since the speed of the thermal wave is considerably smaller than that of the mechanical waves, the latter control the size of the time step. Once deformations begin to localize, the time step drops significantly. This drop in the time step occurs at a lower value of the nominal strain for a particulate composite than that for the homogenized body. This is because inhomogeneities in deformations introduced by numerous particulate/matrix interfaces induce localization, not necessarily simultaneously, of deformation at several discrete points in the body. Eventually the deformation localizes into a connected region. For a 100×100 uniform FE mesh, the CPU time is $\sim$ 300 hr on a SGI single processor Altix machine. The code could not be parallelized because of a lack of a parallel version of LSODE.

3.1 Values of Material Parameters

Values of thermophysical parameters for W and the NiFe are listed in Table 1. Values assigned to other parameters given below in (24) are the same for the two constituents and for the homogenized body; we note that these are not readily available in the literature for different materials.

$$\begin{aligned} &\beta_1 = 1.5,\ \beta_2 = 1.0,\ f_2 = 0.04,\ s_2 = 0.1 \\ &\varepsilon_n = 0.5,\ \tau = 10^{-8}\text{s},\ \theta_r = 273\ \text{K} \\ &f_c = 0.15,\ f_u = 2/3,\ f_f = 0.25 \end{aligned} \tag{24}$$

Thus, the accoustic impedances of W and NiFe equal 87.86×10^6 and 48.44×10^6 kg/(m^{2}s), respectively, and differ by a factor of 1.8. The bar wave speeds in W and NiFe are 4,552 and 5,265 m/s and differ by a factor of 0.86.

Because of the random distribution of W particulates, and the variation of the axial load with time t, the fraction of the axial load supported by W and NiFe at a horizontal surface $x_2 =$ constant varies with t. Once either one or both of these constituents begin to deform plastically, the speeds of incremental elastic waves in them will depend on values of the tangent moduli. There are four nonzero components of the Cauchy stress tensor and the elastic strain tensor giving several elastic moduli for each material that need not vanish simultaneously.

3.2 Verification of Code

The method of ficticious body forces (also called the method of manufactured solutions) is used to verify that the code correctly solves the initial-boundary-vaue problem expressed by Eqs. (1)–(18). In this method, analytical expressions for the displacement and the temperature fields are presumed, and body forces and sources of internal energy [note that these had been set equal to zero in Eqs. (2) and (4)] are computed so as to satisfy the balance of linear momentum and the balance of internal energy. Also, initial and boundary conditions are derived from the assumed displacement and temperature fields. These are input into the code and the numerical solutions are found. A good agreement between the computed and the analytical solutions verifies the code. This method was also used by Batra and Liang [45], e.g., see remarks following Eq. (30) of their paper.

For a shear band problem, computed results were also found to agree very well with those obtained by Batra and Lear [33], who employed a similar problem formulation but with three-node triangular elements.

The code was used to study wave propagation in an inhomogeneous elastic bar [46]. The time histories of the computed wave speed and of the axial stress at a point were found to agree well with the analytical solution of Chiu and Erdogan [47].

TABLE 1. Values of material parameters

Material	ρ(kg/m^3)	E (GPa)	ν	κ (W/(mK))	c (J/(kg K))	$\alpha(10^{-6}/K)$
Tungsten	19,300	400	0.29	160	138	5.3
NiFe	9,200	255	0.29	100	382	15

A(MPa)	B(MPa)	n	C	$\dot{\varepsilon}_0(1/s)$	θ_m(K)	m
730	562	0.075	0.290	10^{-6}	1723	1.0
150	546	0.208	0.0838	10^{-6}	1225	1.0

4. MULTISCALE MODELING

We first analyze the initiation and development of an ASB in a prismatic body of 10 mm × 10 mm square cross section deformed in plane strain tension; cf. Fig. 1(a). The body is made of a homogenized material whose response is equivalent to that of a 50% volume fraction of 50 μm diameter W particulates in the NiFe matrix. As stated earlier, symmetries about the two centroidal axes are exploited, and coupled thermomechanical deformations of the material in the first quadrant are analyzed. The 5 mm × 5 mm region is divided into a uniform 100 × 100 FE mesh of four-node quadrilateral elements. The uniform initial porosity distribution equals 0.025, and it is deformed at a nominal strain rate of 5000/s until plastic deformations have localized into a narrow region. The time histories of unknowns at nodes on the surfaces $X_1 = 1$ mm and $X_2 = 1$ mm in the undeformed configuration are recorded for later use. Subsequently, detailed deformations of the material in the 1 mm × 1 mm region with two edges along the centroidal axes of the original cross section are analyzed. As shown in Fig. 1(b), the 0.5 mm × 0.5 mm region has 50 μm diameter W particulates randomly distributed in the NiFe matrix, and the remaining region is the homogenized material equivalent to the particulate composite and used in the analysis of the 5 mm × 5 mm region. On the surfaces $X_1 = 1$ mm and $X_2 = 1$ mm, the time histories of surface tractions (normal and tangential components of the first Piola-Kirchhoff stress tensor extrapolated from their values at the neighboring Gauss integration points) and of temperature as computed from the previous analysis are applied with the remaining two surfaces having the same boundary conditions as in the original analysis of the 5 mm × 5 mm region.

Numerical experiments with the velocity components and the temperature prescribed on the surfaces $X_1 = 1$ mm and $X_2 = 1$ mm failed to compute the deformation field subsequent to the initiation of the localization of deformation. It seems that the use of a Gurson-type yield surface requires that deformations in the macro- and the micromodels be quite close to one another; otherwise deformations cease to be nearly isochoric and porosity evolution limits the time up to which the numerical solution can be satisfactorily computed. Here, the FE mesh employed for the macroanalysis is too coarse to resolve an ASB. Even for a homogeneous material, the deformation fields in the macro- and the microanalyses are a little bit different. However, these differences are noticeable when the macroanalysis is performed on the homogeneous body and the micro-analysis on the particulate composite. Thus, one should not expect that the velocity field obtained from an analysis of the homogenized body and applied to the boundaries of the region for the microanalysis will yield an accurate solution of the problem. However, with tractions as-

signed on the surfaces $X_1 = 1$ mm and $X_2 = 1$ mm, deformations of these and other particles adapt readily to the constraints imposed by the stiffer W particulates, and the numerical solution progressed smoothly. It should be added that nodes on the top and the right surfaces of the 1 mm × 1 mm mesh coincide with those on the surfaces $X_1 = 1$ mm and $X_2 = 1$ mm in the 5 mm × 5 mm mesh, respectively.

4.1 Verification of the Methodology

The aforementioned approach was used to analyze deformations of a homogeneous body. Figure 2 compares time histories of the temperature and the rate of increase of temperature of a material particle located at the specimen centroid obtained by the two procedures; i.e., (i) deformations of the 5 mm × 5 mm region are analyzed, and (ii) deformations of the 5 mm × 5 mm followed by that of the 1 mm × 1 mm region are scrutinized. The first approach is termed the macroanalysis, and the second the macro-micro analysis. Figure 3 depicts contours of the effective plastic strain at an average axial strain of 0.29 for the two analyses. It is clear that the rate of increase of temperature is much higher in the macro-micro analysis than in the pure macroanalysis. The combined analysis can be viewed as refining the FE mesh and, as shown by Batra and Ko [48] and Batra and Hwang [49], the effective plastic strain rate at the ASB center increases when the FE mesh is refined. The ASB initiates, as signified by the jump in the rate of temperature increase, slightly earlier for the macro-micro analysis as compared to that for the macroanalysis; the difference between the two times is $\sim 7\%$ thereby verifying the approach. The intensely deformed region is significantly narrower for the macro-micro analysis than that for the macroanalysis solely due to the finer FE

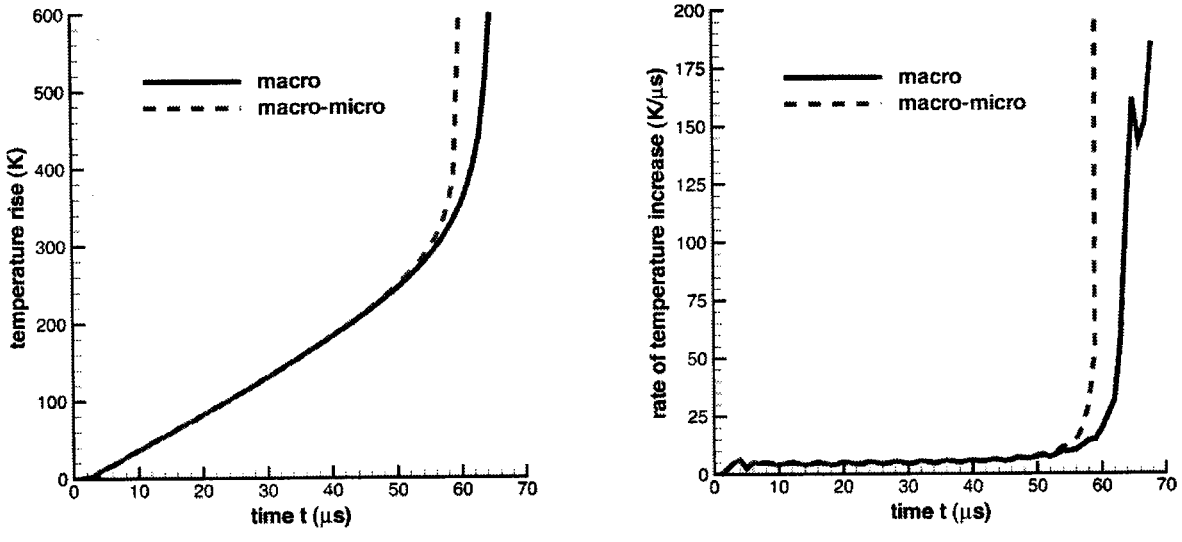

(a) (b)

FIGURE 2. (a) Temperature and (b) rate of increase of temperature versus time at the centroid of a homogeneous (50% W, 50% NiFe) body for the macro and the macro-micro analyses

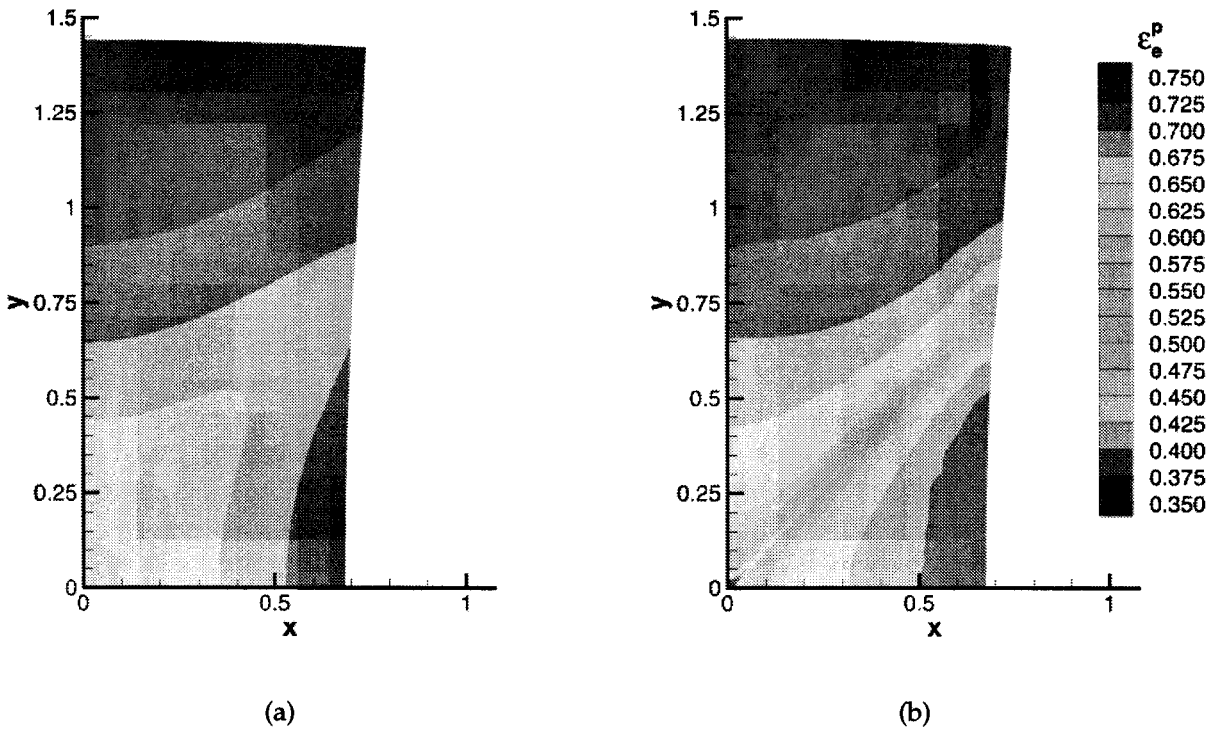

FIGURE 3. Contours of the effective plastic strain for a homogeneous 50/50 W/NiFe sample at $t = 60$ μs for $X_1 \leq 1$ mm and $X_2 \leq 1$ mm for the (a) macro-scale analysis and (b) macro-micro analysis

mesh. In Figs. 3(a) and 3(b), the right edge is not straight because it is an inner surface in the 5 mm × 5 mm cross section. For the same reason, at any time t, the average axial strain in this 1 mm × 1 mm region need not equal the average axial strain in the 5 mm × 5 mm region since the 5 mm × 5 mm region is not deformed homogeneously. This macro-micro analysis could be repeated several times to fully resolve an ASB.

4.2 Results for the Particulate Composite

The above described procedure was applied to four different (three random and one ordered) distributions of 50 μm diameter W particulates in the 0.5 mm × 0.5 mm region. Figure 4 depicts contours of the effective plastic strain and Fig. 5 depicts contours of the rate of increase of temperature for the four distributions. It is evident that deformations localize in different regions and an ASB initiates from a different point in each case. Furthermore, only one of these regions of intense plastic deformation agrees with the general shape of the intensely deformed region in the equivalent homogeneous body. The ASB center can be located from a visual inspection of the contour plots of Figs. 4 and 5; its location does not coincide with the origin or the specimen centroid. The inhomogeneities induced by the presence of W particulates strongly influence where and when an ASB initiates. For the four distributions of W particulates, we have plotted in Fig. 6 time his-

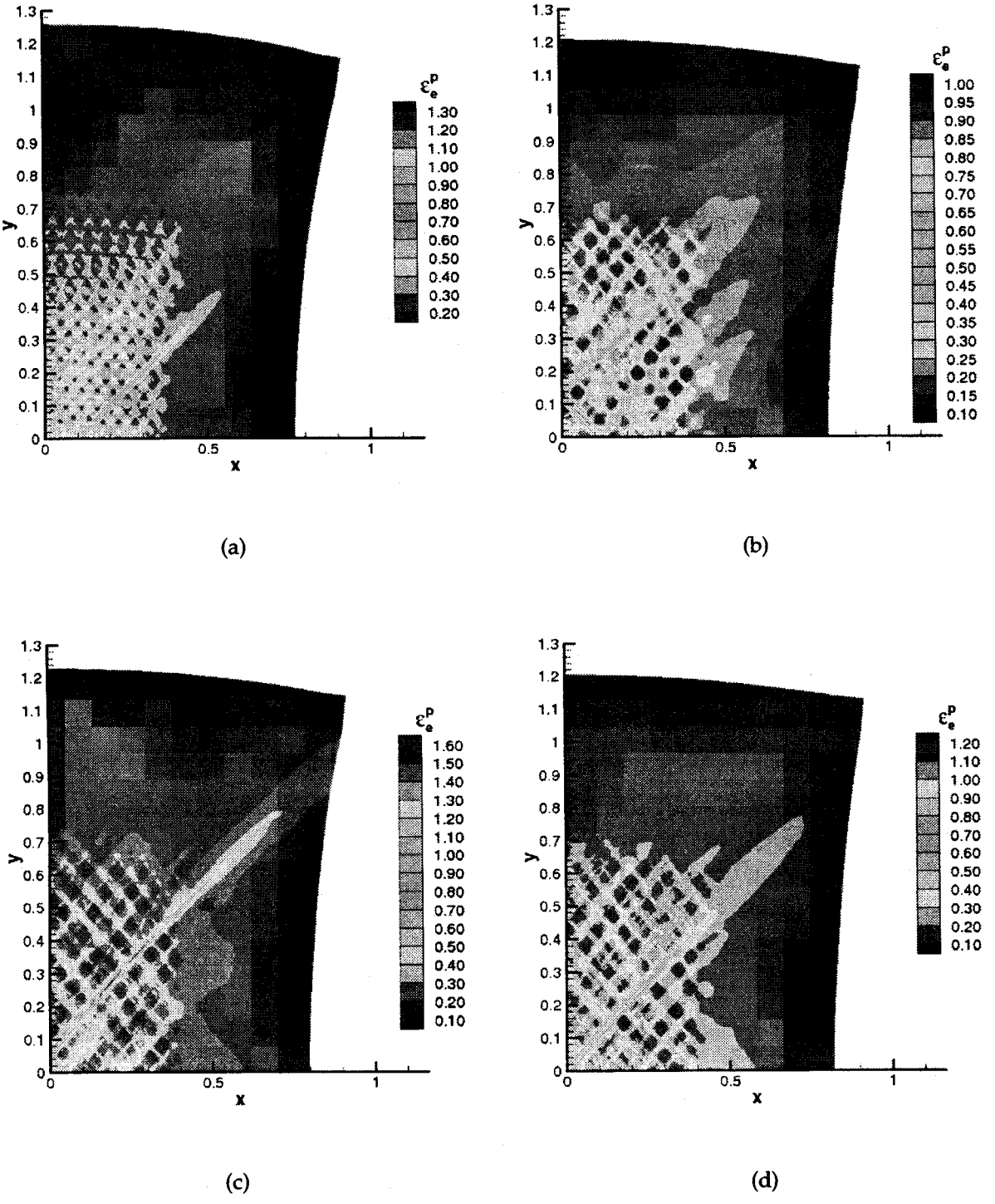

FIGURE 4. Contours of the effective plastic strain at $t = 25.0$ μs for (a) an ordered particulate arrangement and (b)-(d) three random particulate arrangements

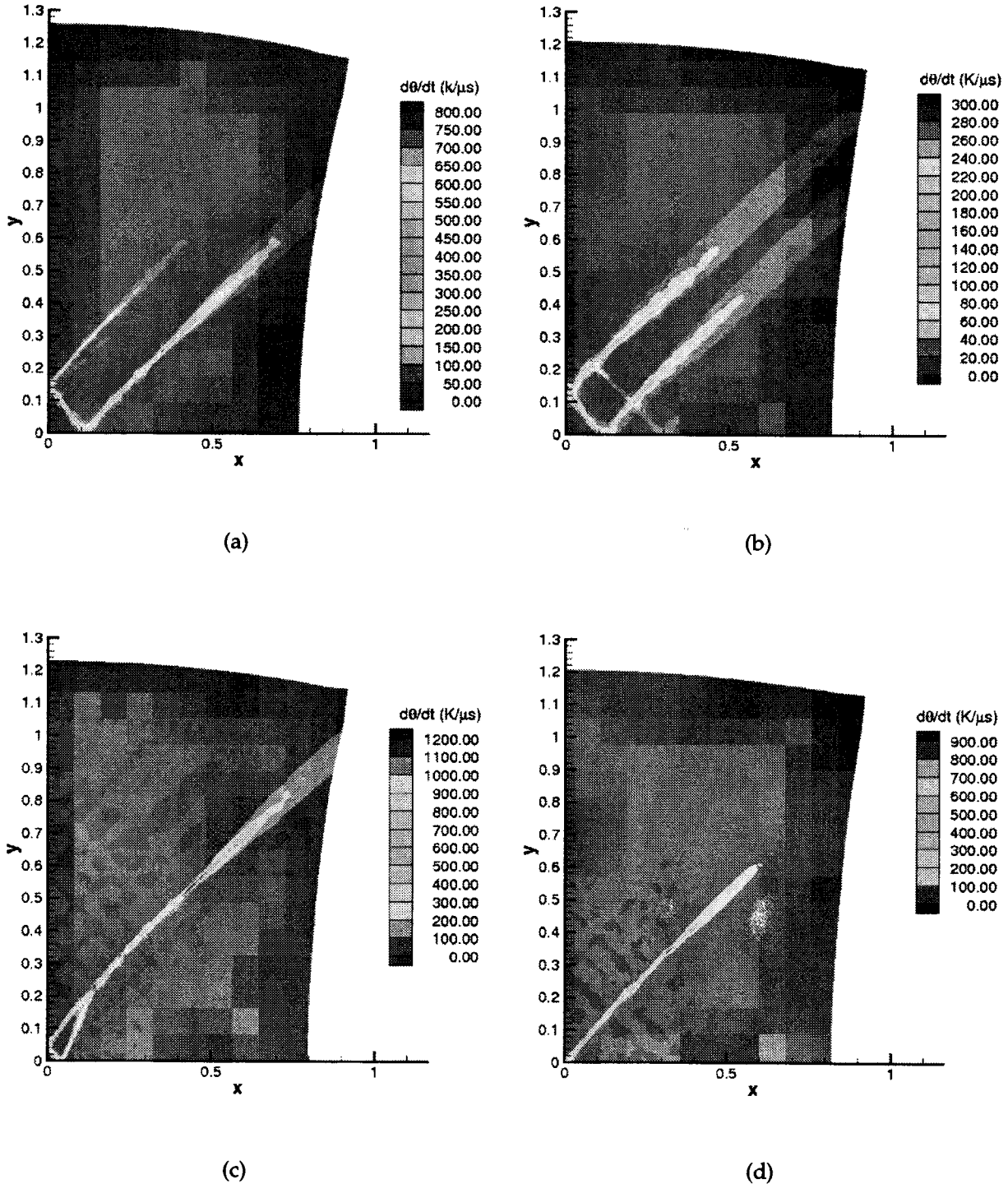

FIGURE 5. Contours of the rate of increase in temperature at $t = 25.0$ μs for (a) an ordered particulate arrangement and (b)-(d) three random particulate arrangements

tories of the rate of temperature rise and of the effective plastic strain at the ASB center. The ordered and the three random distributions of particulates give ASB initiation times between 22 and 24 μs, which is considerably less than the nearly 58 μs (cf. Fig. 2) deduced from the analysis of deformations of the equivalent homogenized body. The large difference between the two values cannot be attributed to the considerably finer mesh employed in the microanalysis; the reasons are a subject for future investigations. An alternative technique found subsequently that considers the microstructure and still gives good values of the ASB initiation time but not necessarily of its origination point is described in Ref. [56]. The deformed configurations at $t = 25$ μs plotted in Fig. 5 suggest that the nominal axial strains for the three random distributions are essentially the same, but are slightly less than that for the ordered distribution of particulates.

For comparison, we also analyzed plane strain thermomechanical deformations of the 0.5 mm × 0.5 mm region containing 50% volume fraction of randomly distributed 50 μm diameter W particulates with the right edge $X_1 = 0.5$ mm traction free and the top surface $X_2 = 0.5$ mm pulled at 2.5 m/s. Figures 7(a) and 7(b) exhibit fringe plots of the axial velocity and of the rate of change of temperature at $t = 60$ μs. It is evident that during the deformation process the right edge does not remain straight because of the distinctly different deformations of the W particulates and the NiFe matrix. The time history of the rate of temperature increase at the ASB center, not exhibited here, reveals that the ASB initiates at ∼ 50 μs. However, the time when the ASB has developed strongly depends on the arrangement of the W particulates; for example, the ASB developed at ∼ 60, 70, and 90 μs for three different random distributions of the W particulates. We note that these times are much larger than the ∼ 25 μs obtained from the multiscale analysis of the problem.

A reason for the large difference in the ASB initiation times for the homogenized and the particulate composites is that waves of large

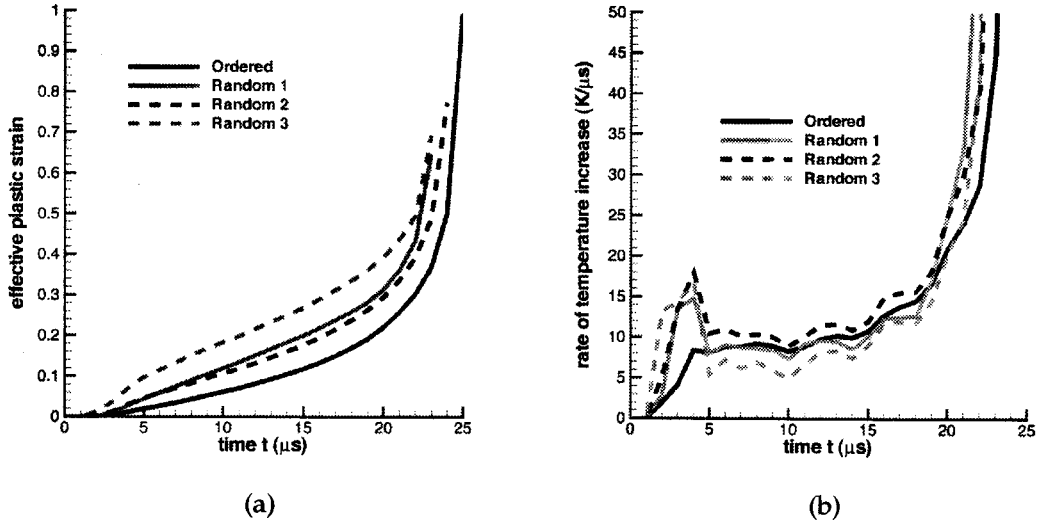

(a) (b)

FIGURE 6. (a) Effective plastic strain and (b) rate of temperature increase at a point inside the ASB as functions of time for four particulate arrangements

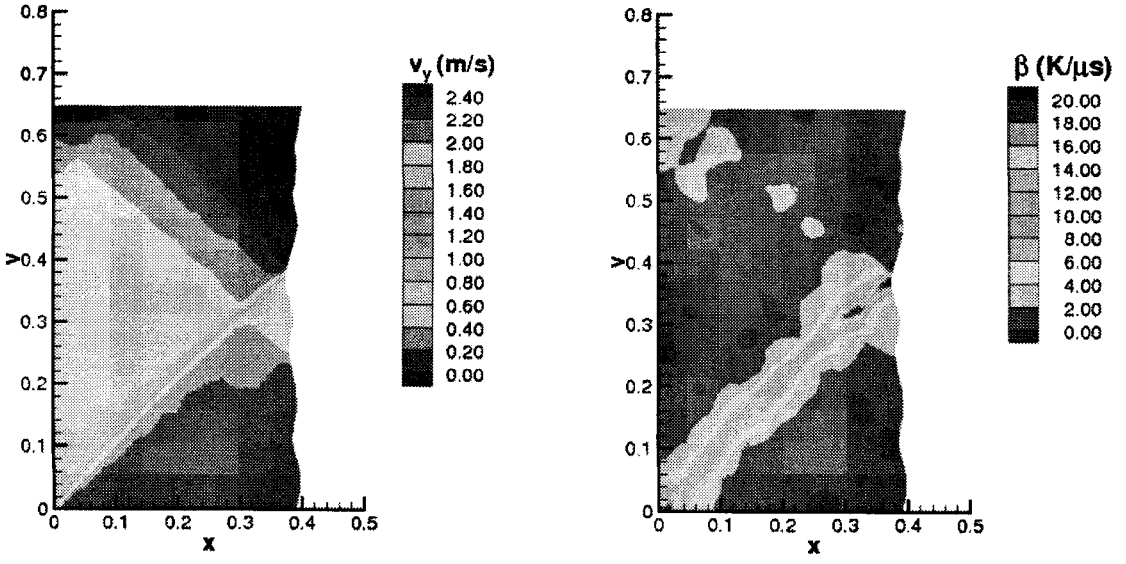

FIGURE 7. At $t = 60$ μs, fringe plots of (a) the axial velocity, and (b) the rate of change of temperature

wavelengths propagate through the homogenized body but waves of small wavelengths probably predominate in the particulate composite. The wavelengths in the particulate composite are influenced by the mismatch in the acoustic properties of the particulates and the matrix materials, and also by the distance between any two adjacent particulates.

4.3 Effects of Particulate Size and Shape

Since values of material parameters for the equivalent homogenized body derived from the rule of mixtures are independent of the size and shape of particulates, the ASB initiation time computed from the analysis of deformations of the homogenized body will not depend on the size and shape of particulates. However, for other than circular particulates, the response of the equivalent homogeneous body is likely to be anisotropic. It is reasonable to expect that particulate shape will influence the ASB initiation time. Also, all particulates need not be identical; such problems will be analyzed in the future.

4.4 Effect of the FE Mesh

Because of the nearly 300 hours of CPU time needed for analyzing one problem, numerical experiments with different FE meshes could not be performed. However, in an inhomogeneous thermoviscoplastic body with a continuous spatial variation of material properties varying continuously, results [9] for the ASB initiation time for three uniform FE meshes are described in Table 2. It is evident that the ASB initiation time decreased by 2.1% in going from a 40×40 to a 120×120 uniform mesh, and the CPU time increased by a factor of 21.

TABLE 2. Effect of FE mesh on the ASB initiation time in an inhomogeneous thermoviscoplastic body

Uniform FE mesh	ASB initiation time (μs)	CPU time (secs)	% change in ASB initiation time
40 × 40	65.9	1,133	—
80 × 80	64.8	6,908	1.67
120 × 120	64.5	29,242	2.12

One way to reduce the effect of the element size on computed results is to use a strain-rate gradient-dependent viscoplasticity theory such as that employed by Batra [50]. It introduces additional material parameters whose values are not readily available in the literature.

4.5 Effect of Strain Gradients

Dai *et al.* [51] used the split-Hopkinson bar to analyze torsional deformations of a SiC/Al (silicon carbide/aluminum) particulate composite. They found that an ASB formed in the composite with 2 μm diameter SiC particulates, but not with 6 μm diameter SiC particulates. They conjectured that strain gradients were higher for the smaller size particulates and these promoted the initiation of ASBs. Furthermore, they explained this by assuming that the flow stress in shear depends on the strain gradients. However, they did not consider higher-order stresses conjugate to the strain gradients as had been done by Batra [49] and Batra and Kim [52]. These two investigations show that consideration of strain gradients and the corresponding higher-order stresses delay the initiation of an ASB. Certainly, its resolution needs additional experimental, analytical, and numerical work.

4.6 Adiabatic Shear Band Initiation Criterion

In several previous studies on the initiation and propagation of ASBs in homogeneous materials, some of which are summarized by Batra [53], it was assumed that an ASB initiates when the maximum shear stress or the maximum effective stress at a point has dropped to 80% of its peak value at that point. This criterion when applied to particulate composites failed [54] because it indicated, not necessarily simultaneously, the initiation of an ASB at numerous discrete points whose spatial locations varied with the random distribution of W particulates in the NiFe matrix. Because of the heat and the load exchange between the particulates and the matrix, the effective plastic strain need not increase monotonically at a point including that where an ASB has initiated. Numerical experiments have indicated that once the total load required to deform the body has dropped to 80% of its peak value, a coherent ASB develops. The rate of temperature increase within this contiguous shear banded region is at least an order of magnitude higher than that in the surrounding regions. Also, the axial velocity has very sharp gradients across the shear banded region. We note that the ASB initiation criterion in terms of the drop in the total load provides no information about the point where the ASB initiates, and cannot be used to analyze the propagation, and hence to compute the speed of the ASB.

We note that Batra and Peng [55] analyzed plane strain transient thermomechanical deformations of a WHA and depleted uranium by modeling each material as homogeneous and isotropic. They introduced numerous randomly distributed weak elements in the uniform FE mesh. It was found that differences in the values of the shear moduli of the two materials accounted for the different orientations of ASBs in them.

5. CONCLUSIONS

We have studied the development of an adiabatic shear band in particulate composites, using plane strain tension tests on the equivalent homogenized body, a multiscale analysis on the particulate composite, and an analysis of deformations of the composite body comprised of particulates and the matrix. It is found that the initiation and propagation of ASBs in particulate composites is decidedly different from that in a homogeneous material; particulate/matrix interfaces act as defects, introduce strong inhomogenities into the deformations, and promote the formation of ASBs. The ASB initiation time computed from the multiscale analysis is considerably less than that obtained from the macroscale analysis of either the equivalent homogenized body or the individual constituents. The location of the ASB center and the shapes of regions where the deformations have localized strongly depend on the arrangement of particulates. Contours of the rate of change of temperature and of the axial velocity, rather than contours of the effective plastic strain, facilitate the delineation of ASBs. The ASB initiation criterion applicable to homogeneous materials fails for particulate composites. The time when the total axial load has dropped to 80% of its peak value indicates when the ASB has developed, but provides no information about its point of initiation.

ACKNOWLEDGMENT

This work was partially supported by NSF Grant No. CMS0002849, ONR Grants No. N00014-98-1-0300 and No. N00014-03-MP-2-0131, ARO Grant No. DAAD19-01-1-0657, and AFOSR MURI to Georgia Institute of Technology with a subcontract to Virginia Polytechnic Institute and State University. Views expressed in the paper are those of the authors and not of the funding agencies.

REFERENCES

1. Bai, Y. L., and Dodd, B., *Adiabatic Shear Localization: Occurence, Theories, and Applications*. Pergamon Press, Oxford, 1992.
2. Wright, T. W., *The Physics and Mathematics of Adiabatic Shear Bands*. Cambridge University Press, Cambridge, 2002.
3. Perzyna, P., Ed., *Localization and Fracture Phenomenon in Inelastic Solids*. Springer-Verlag, Berlin, 1998.
4. Batra, R. C., and Zbib, H. M., Eds., *Material Instabilities: Theory and Applications*. ASME, New York, 1994.
5. Tomita, Y., Simulation of plastic instabilities in solid mechanics, *Appl. Mech. Rev.* **47**:171–205, 1994.
6. Armstrong, R., Batra, R. C., Meyers, M., and Wright, T. W., Eds., Shear instabilities and viscoplasticity theories, *Mechs. of Materials* **17**:83–328, 1994.
7. Batra, R. C., Rajapakse, Y. D. S., and Rosakis, A., Eds., Failure mode transitions under dynamic loading, *Int. J. of Fracture* **101**:1–180, 2000.
8. Zbib, H. M., Shawki, T., and Batra, R. C., Eds., Material instabilities, *Appl. Mech. Rev.* **45**:1–173, 1992.
9. Batra, R. C., and Love, B. M., Adiabatic shear bands in functionally graded materials, *J. Thermal Stresses* **27**:1101–1123, 2004.
10. Charalambakis, N., and Baxevanis, T., Adiabatic shearing of non-homogeneous thermoviscoplastic materials, *Int. J. Plasticity* **20**:899–914, 2004.
11. Zhou, M., Needleman, A., and Clifton, R. J., Finite element simulations of dynamic shear localization, *J. Mech. Phys. Solids* **42**:423–458, 1994.
12. Zhou, M., and Clifton, R. J., Dynamic constitutive and failure behavior of a two-phase tungsten composite. ASME *J. Appl. Mech.* **64**:487-494, 1997.
13. Bose, A., Congue, H., and Lankford, Jr. J., Influence of microstructure on shear localization in tungsten heavy alloys. In: *Proceedings of the First International Conference on Tungsten and Tungsten Alloys*, November 15–18, Bose, A., Dowding, R. J., Eds., Metal Powder Industries

Federation, Arlington, VA, 291–298, 1992.

14. Kim, D. K., Lee, S., and Song. H. S., Effect of tungsten particle shape on dynamic deformation and fracture behavior of tungsten heavy alloys, *Metall. Mater. Trans. A* **29**:1057–1069, 1998.
15. Wei, Z., Yu, J., Li, J., Li, Y., and Hu, S., Influence of stress condition on adiabatic shear localization of tungsten heavy alloys, *Int. J. Impact Eng.* **26**:843–852, 2001.
16. Dick, R. D., Ramachandran, V., Williams, J. D., Armstrong, R. W., Holt, W. H., and Mock, Jr. W., Dynamic deformation of W7Ni3Fe alloy via reverse-ballistic impact. In *Tungsten and Tungsten Alloys-Recent Advances*. Crowson, A., and Chen, E. S., Eds., The Minerals, Metals & Materials Society, Ohio, 269–276, 1991.
17. Batra, R. C., and Wilson, N. M., Adiabatic shear bands in plane strain deformations of a WHA, *Int. J. Plasticity* **14**:43–60, 1998.
18. Stevens, J. B., and Batra, R. C., Adiabatic shear bands in the Taylor impact test for a WHA rod, *Int. J. Plasticity* **14**:841–854, 1998.
19. Zhou, M., The growth of shear bands in composite microstructures, *Int. J. Plasticity* **14**:733–754, 1998.
20. Ghoneim, N. M., Busso, E. P., Kioussis, N., and Huang, H. C., Multiscale modelling of nanomechanics and micromechanics: an overview, *Phil. Mag.* **83**:3475–3528, 2003.
21. Belak, J., Multi-scale applications to high strain-rate dynamic fracture, *J. Computer-Aided Mater. Des.* **9**:165–172, 2002.
22. Kadowaki, H., and Liu, W. K., Bridging multiscale method for localization problem, *Compt. Methods Appl. Mech. Eng.* **193**:3267–3302, 2004.
23. Batra, R. C., and Jaber, N. A., Failure mode transition in an impact loaded prenotched plate with four thermoviscoplastic relations, *Int. J. Fracture* **110**:47–71, 2001.
24. Gurson, A. L. Continuum theory of ductile rupture by void nucleation and growth: Part I, ASME *J. of Engr. Mater. Technol.* **99**:2-15, 1977.
25. Tvergaard, V., Influence of voids on shear band instabilities under plane strain conditions, *Int. J. Fracture* **17**:389–407, 1981.
26. Johnson, G. R., and Cook, W. H., A constitutive model and data for metals subjected to large strains, high strain-rates, and high temperatures, *In Proc. 7th Int'l. Symp. on Ballistics*, The Hague, The Netherlands, 541–547, 1983.
27. Chu, C., and Needleman, A., Void nucleation in biaxially stretched sheets, *J. Eng. Mat. Technol.* **102**:249–256, 1980.
28. Tvergaard, V., and Needleman, A., Analysis of the cup-cone fracture in a round tensile bar, *Acta Metall.* **32**:157–169, 1984.
29. Budiansky, B., Thermal and thermoelastic properties of isotropic composites, *J. Compos. Mater.* **4**:701–744, 1990.
30. Jiang, B., and Batra, R. C., Effective properties of a piezocomposite containing shape memory alloy and inert inclusions, *Continuum Mech. Thermodyn.* **14**:87–111, 2002.
31. Cattaneo, C., A form of the heat equation which eliminates the paradox of instantaneous propagation, *CR Acad. Sci.* **247**:431–433, 1958.
32. Vernotte, P., The true heat equation, *CR Acad. Sci.* **247**:2103–2105, 1958.
33. Batra, R. C., and Lear, M. H., Adiabatic shear banding in plane strain tensile deformations of eleven thermoviscoplastic materials with finite wave speed, *Int. J. Plasticity* **21**:1521–1545, 2005.
34. Batra, R. C., and Chen, L., Instability analysis and shear band spacing in gradient-dependent thermoviscoplastic materials with finite speeds of thermal waves, *Arch. Mech.* **53**:167–192, 2001.
35. Batra, R. C., On heat conduction and wave propagation in non-simple rigid solids, *Lett. Appl. Eng. Sci.* **3**:97–107, 1975.
36. Batra, R. C., and Kim, K. H., Effect of viscoplastic flow rules on the initiation and growth of shear bands at high strain rates, *J. Mech. Phys. Solids* **38**:859–874, 1990.
37. Batra, R. C., and Chen, L., Effect of viscoplastic relations on the instability strain, shear band initiation strain, the strain corresponding to maximum shear band spacing, and the band width in a thermoviscoplastic material, *Int. J. Plasticity* **17**:1465–1489, 2001.
38. Batra, R. C., Steady state penetration of thermoviscoplastic targets, *Comput. Mech.* **3**:1–12, 1988.
39. Bodner, S. R., and Partom, Y., Constitu-

tive equations for elastic-viscoplastic strain-hardening materials. ASME *J. Appl. Mech.* **56**:385–389, 1975.

40. Hill, R., A self consistent mechanics of composite materials, *J. Mechs. Phys. Solids* **13**:213–222, 1965.
41. Mori, T., and Tanaka, K., Average stress in matrix and average elastic energy of materials with misfitting inclusions, *Acta Metal.* **21**:571–574, 1973.
42. Suquet, P., Overall potential and extremal surfaces of power law or ideally plastic composites, *J. Mech. Phys. Solids* **41**:981–1002, 1993.
43. Hughes, T. J. R., *The Finite Element Method, Linear Static and Dynamic Finite Element Analysis*, Prentice-Hall, Englewood Cliffs, 1987.
44. Batra, R. C., Finite plane strain deformations of rubberlike materials, *Int. J. Numer. Methods Eng.* **15**:145–160, 1980.
45. Batra, R. C., and Liang, X. Q., Finite deformations of smart structures, *Comput. Mech.* **20**:427–438, 1997.
46. Batra, R. C., and Love, B. M., Crack propagation due to brittle and ductile failures in microporous thermoelastoviscoplastic functionally graded materials, *Eng. Fract. Mech.* **72**:989–1014, 2005.
47. Chiu, T. C., and Erdogan, F., One-dimensional wave propagation in a functionally graded medium, *J. Sound Vibr.* **222**:453–487, 1999.
48. Batra, R. C., and Ko, K. I., An adaptive mesh refinement technique for the analysis of shear bands in plane strain compression of a thermoviscoplastic solid, *Comput. Mech.* **10**:369–379, 1992.
49. Batra, R. C., and Hwang, J., An adaptive mesh refinement technique for two-dimensional shear band problems, *Comput. Mech.*, **12**:255–268, 1993.
50. Batra, R. C., The initiation and growth of, and the interaction among adiabatic shear bands in simple and dipolar materials, *Int. J. Plasticity* **3**:75–89, 1987.
51. Dai, L. H., Liu, L. F., and Bai, Y. L., Formation of adiabatic shear bands in metal matrix composites, *Int. J. Solids Struct.* **41**:5979–5993, 2004.
52. Batra, R. C., and Kim, C. H., Adiabatic shear banding in elastic-viscoplastic nonpolar and dipolar materials, *Int. J. Plasticity* **6**:127–141, 1990.
53. Batra, R. C., Numerical Solution of Initial-Boundary-Value Problems with Shear Strain Localization in *Localization and Fracture Phenomenon in Inelastic Solids*. Perzyna, P., Ed., Springer-Verlag, Berlin, 301–389, 1998.
54. Batra, R. C., and Love, B. M., Mesoscale analysis of shear bands in high strain rate deformations of tungsten/nickel-iron composites, *J. Thermal Stresses*, **28**:747–782, 2005.
55. Batra, R. C., and Peng, Z., Development of shear bands in dynamic plane strain compression of depleted uranium and tungsten blocks, *Int. J. Impact Eng.*, **16**:375–395, 1995.
56. Batra, R. C., and Love, B. M., Consideration of microstructural effects in the analysis of adiabatic shear bands in a tungsten heavy alloy, *Int. J. Plasticity*, (in press, available online).